Schaber, C.; Flenner, S.; Glisovic, A.; Krasnov, I.; Rosenthal, M.; Stieglitz, H.; Krywka, C.; Burghammer, M.; Müller, M.; Gorb, S.:
Hierarchical architecture of spider attachment setae reconstructed from scanning nanofocus X-ray diffraction data.
In: Journal of the Royal Society Interface. Vol. 16 (2019) 150, 20180692.

First published online by The Royal Society: 30.01.2019

https://dx.doi.org/10.1098/rsif.2018.0692

Hierarchical architecture of spider attachment setae reconstructed from scanning nanofocus X-ray diffraction data

Clemens F. Schaber[1], Silja Flenner[2,3], Anja Glisovic[3], Igor Krasnov[3], Martin Rosenthal[4], Hergen Stieglitz[2,3], Christina Krywka[2], Manfred Burghammer[4], Martin Müller[2,3], Stanislav N. Gorb[1]

[1] Functional Morphology and Biomechanics, Zoological Institute, Kiel University, 24098 Kiel, Germany

[2] Helmholtz-Zentrum Geesthacht, Postfach 1160, 21494 Geesthacht, Germany

[3] Institute of Experimental and Applied Physics, Kiel University, 24098 Kiel, Germany

[4] European Synchrotron Radiation Facility (ESRF), CS 40220, 38043 Grenoble Cedex 9, France

Authors for correspondence:

C. F. Schaber

e-mail: cschaber@zoologie.uni-kiel.de

M. Müller

e-mail: martin.mueller@hzg.de

Abstract

When sitting and walking, the feet of wandering spiders reversibly attach to many surfaces without the use of gluey secretions. Responsible for the spiders' dry adhesion are the hairy attachment pads that are built of specially shaped cuticular hairs (setae) equipped with approximately 1 μm wide and 20 nm thick plate-like contact elements (spatulae) facing the substrate. Using synchrotron-based scanning nanofocus X-ray diffraction methods, combining wide-angle X-ray diffraction/scattering (XRD/WAXS) and small-angle X-ray scattering (SAXS), allowed for gaining substantial quantitative information about the structure and materials of these fibrous adhesive structures with 200 nm resolution. The fibre diffraction patterns showed the crystalline chitin chains oriented along the long axis of the attachment setae and increased intensity of the chitin signal dorsally within the seta shaft. The small-angle scattering signals clearly indicated an angular shift by approximately 80° of the microtrich structures that branch off the bulk hair shaft and end as the adhesive contact elements in the tip region of the seta. The results reveal the specific structural arrangement and distribution of the chitin fibres within the attachment hair's cuticle preventing material failure by tensile reinforcement and proper distribution of stresses that arise upon attachment and detachment.

Keywords:

chitin, cuticle, hair, fibrous adhesive structures, fibre diffraction, small-angle X-ray scattering (SAXS), wide-angle X-ray diffraction/scattering (XRD/WAXS)

1. Introduction

Wandering spiders, such as the large Central American spider *Cupiennius salei*, are able to climb vertically and walk upside down on smooth and rough surfaces [1–4]. They share this capability with many insects such as e.g. flies and beetles. However, some mechanisms underlying the strong adhesion between the animals' feet and a substrate are different in insects and spiders. Insect adhesion relies on capillary forces caused by fluid secretions between their attachment structures and the substrate [5–9]. Wandering spiders are assumed to adhere due to van der Waals forces between their attachment setae and the substrate without additional fluid involved. This mechanism is generally termed dry adhesion and well-studied in the gecko [10–16] and spider [2,17,18] attachment systems. These dry adhesive systems recently have also been the model for many biomimetic structural adhesives [19–29].

However, although some of the artificial adhesive hair-like structures can reach higher adhesive strength than the natural models, particularly on smooth surfaces, the artificial structured adhesives do not reach the performance of their biological prototypes in regard to their durability and their adaptedness to substrates with a wide range of surface properties, such as e.g. different roughness or surface energies. One of the reasons might be inhomogeneously distributed materials within the biological models, as previously shown in the wet fibrous attachment system of beetles [30]. For dry fibrous attachment systems, the possible distribution of materials with different mechanical properties has not been examined previously. This is why in the present paper, the spider attachment hairs were selected as model system for synchrotron-based X-ray diffraction studies of the materials involved. Since additional fluid interactions can be excluded, the spider setae are also attractive for X-ray *in situ* examination of the attachment process.

The spider *Cupiennius salei* is a widely studied spider species and has been a model organism for neurobiology, mechanoreception, sensory physiology, biomechanics, and its exoskeleton´s structure, function, and mechanical properties (see, e.g. [31–34]). During its eight-legged locomotion, *Cupiennius salei* moves the diagonally opposing legs simultaneously. In quickly walking spiders (10 cm/s), the most prominent ipsilateral (one sided) sequence of the legs contacting the ground is 4-2-1-3. However, dependent on the actual substrate and velocity, a wide variety of leg movement patterns can be found. Also, the spiders are able to very quickly compensate the loss of legs by adaptation of their gait pattern [31]. It was shown that each single foot of *Cupiennius salei* can provide 12 mN adhesion force in intact eight-legged animals and approximately 35 mN friction force [35].

Apart from attachment hairs, many other, mostly sensory, hair-shaped cuticular structures such as tactile, wind-sensing, and proprioreceptive setae of the spider *Cupiennius salei* were previously studied in detail [36–39], pointing on the great diversity and versatility of the apparently simple building principle of an arthropod cuticular hair. Since the real hairs of mammals are made of keratin and evolved completely different from the cuticular hairs of arthropods, the correct anatomical term for a cuticular hair-like structure in zoology is seta (*pl.* setae). However, we use both terms synonymously in the present study.

The pretarsal hairy attachment structures of the spider *Cupiennius salei* are called the claw tuft or pretarsal scopula [4,40], which comprises approximately 1,000 setae located at the distal end of each leg in between of two claws that are used for clamping on rough surfaces. The attachment setae are 200 μm to 800 μm long, dependent on the exact location in the claw tuft. The surface of the attachment hairs is covered with thousands of cuticular protuberances, the so-called microtrichs, branching off the shaft of each seta. In the adhesive tip region of the seta these microtrichs are highly ordered in up to 20 parallel rows and point away from the shaft backbone at an angle of about 80° (figure 1*a*,*b*). Here, the microtrichs consist of narrowing stalks that emerge from the shaft backbone and terminate in approximately 1 μm wide and 20 nm thin spatula-shaped plates, which are the contact elements responsible for the formation of intimate contact with the surface of a substrate and the enhancement of adhesion [3,41] (figure 1*c*).

The exoskeleton of spiders and thus the attachment setae are made of cuticle, a compound material that consists mainly of proteins and reinforcing polymeric chitin fibres [42]. Chitin is a polysaccharide of (1,4) linked 2-deoxy-2-acetamido-β-D-glucose units [43] and arranged in crystalline chains [44]. It is detectable using wide-angle X-ray diffraction by its characteristic fibre diffraction pattern. Among several chitin subtypes, the one found in arthropods is α-chitin, which is identified by two antiparallel polymer chains arranged helicoidally and an orthorhombic unit cell. Previous studies confirmed the presence of α-chitin in the cuticle of the spider *Cupiennius salei* [45–47]. In the exoskeleton of arthropods, chitin molecules are arranged in nanofibrils, each consisting of 18 to 25 single chitin chains. These nanofibrils are approximately 2 – 5 nm thick and 300 nm long. They are embedded in a matrix of structural proteins forming chitin-protein fibres with typical diameters of 50 – 350 nm [48,49].

In order to obtain more information about the distribution of chitin in the spider attachment hairs and to characterise the structures responsible for the remarkable attachment

capabilities of the spider, we mapped the information gained by using synchrotron-based scanning nanofocus X-ray diffraction on distal sections of single attachment setae including the adhesive tip. Wide-angle X-ray scattering (WAXS) patterns allowed us for specifically mapping the distribution of chitin in the different structures of the adhesive seta. Additionally, we obtained data about the orientation of the chitin fibrils. The analysis of the small-angle X-ray scattering (SAXS) signals gave us insights in the distribution and orientation of mesoscopic structures with the size of approximately 100 nm. The main advantage of the methods used over light and electron microscopic techniques was that no further chemical or mechanical sample treatment potentially introducing artefacts was necessary, except mounting of the samples on sample holders suitable for the scanning nanofocus X-ray diffraction setups.

2. Materials and Methods

2.1. Sample preparation

Single attachment hairs (setae) were picked from second and third walking legs of specimens of the spider *Cupiennius salei* (Ctenidae) in the middle of the pretarsal claw tuft. The animals were obtained from the breeding stock of the Department of Neurobiology of the University of Vienna, Austria. Most results were gained from hairs of legs separated from the spider not longer than five days prior to the experiment and kept in a fridge whenever possible. In this case the legs were sealed at their autotomy site on the trochanter using a slightly heated mixture of beeswax and colophony. Single hairs were glued free-standing onto the tip of a sharpened glass capillary using two-component polysiloxane (Coltene light body, Coltène/Whaledent AG, Altstätten, Switzerland) prior to exposure. Some other samples were taken from legs frozen at -20° C for one month and mounted on 200 µm thick frames of Si_3N_4 sample windows (Norcada Inc., Edmonton, Canada; without membrane) three days before the experiments.

2.2. Scanning nanofocus X-ray diffraction

The experiments were performed at the nanofocus extension EH III of the beamline ID13 at the European Synchrotron Research Facility ESRF (Grenoble, France) and the Nanofocus Endstation (operated by Helmholtz-Zentrum Geesthacht and Kiel University) of the MiNaXS-beamline P03 [50] of PETRA III at the Deutsches Elektronen-Synchrotron DESY (Hamburg, Germany). At the ESRF, an Eiger X 4M detector (Dectris Ltd., Baden-Daetwill, Switzerland) was set up at a distance of 203.5 mm to the sample. The distance between the 400 µm thick cylindrical beamstop downstream the sample and the detector was bridged by a helium-filled flight-tube. The wavelength of the X-ray beam focused to a size of 150 × 150 nm^2 was 0.847 Å. The maximum lateral resolution of the scanning setup was set to 200 nm, and data were acquired with exposure times of 1 s. At PETRA III, a Pilatus 1M detector (Dectris Ltd., Baden-Daetwill, Switzerland) was placed at a distance to the sample of 184.2 mm. The wavelength of the X-ray beam sized approximately 400 × 400 nm^2 was 0.950 Å. Lateral resolution of

the scanning setup was set to 1 µm at exposure times of 35 s per step. The intensity of the X-ray beam on the sample at PETRA III at the time of the experiments was supposed to be 10–20 times lower that at the ESRF. Data was evaluated using the software package FIT2D (A. P. Hammersley, ESRF, Grenoble, France) and the Python library pyFAI (Data analysis unit, ESRF, Grenoble, France). For quantitative analyses of both the signal intensity and orientation, the two-dimensional diffraction data was converted by azimuthal integration into one-dimensional profiles as function of the scattering vector q. In total, data were recorded from 17 setae from seven legs of seven different animals, and the most representative examples were selected for presentation.

3. Results

3.1. X-ray diffraction patterns

The fibre diffraction pattern of α-chitin and a circular halo with a maximum intensity in the range of q between 13 nm^{-1} and 16 nm^{-1} were the two prominent features of the wide-angle X-ray diffraction signals (figure 2). Except for a slight angular shift of orientation caused by the slight curvature of the sample, the averaged chitin diffraction patterns of hair shaft and the transition zone located between the shaft and the tip region (Fig. 1*a*) were very similar and showed the same reflections (figure 2*a*,*b*). There were two broad 020 and 110 reflections on the equator of the diffraction patterns. Of the four reflections off the equator, the 012 and 013 were the most intensive ones. The sharp 001 and 004 meridional reflections were the result of tilt of the chitin crystals with respect to the X-ray beam. In the tip region, only the 012, 013, and the equatorial 020 reflections could be clearly identified. However, there was an additional, intense, and azimuthally widened reflection at q = 14.83 nm^{-1} in the tip, and a weaker one at q = 13.90 nm^{-1} in the shaft. No such distinct additional reflection was found in the transition zone (figure 2).

The origin of the diffuse halo in between q of approximately 12 nm^{-1} to 20 nm^{-1} could not be determined with absolute certainty. For further quantitative analysis and intensity mapping, the integration range for the halo was limited from 13 nm^{-1} to 16 nm^{-1}. This range clearly excluded the 012 and 013 chitin reflections, however included most of the equatorial 110 chitin reflection and the additional non-chitin signals (figures 2*b,c*). Consequently, these integration results were addressed a mixed signal of yet unidentified amorphous material and chitin. A similar superposition of signals of different origin applied to the chitin 012 and 013 peaks that were superimposed by the boundaries of the halo, and the 110 reflection which widely overlapped with the most intense region of the halo. In case of the 013 reflection, the

peak-to-halo relation was largest, and this is why it was used as indicator for the presence of chitin further in this study.

Significant differences of the equatorial 020 chitin peak were found in the different regions of the seta. Compared to shaft and transition zone, the peak from the tip region was broader and shifted to smaller *q*-values (figure 3). Estimating crystal diameter using the Scherrer equation [51] on the positions and widths of the Lorentz fits of the 020 reflections yielded minimum crystal sizes of 2.59 nm ± 0.02 nm for the tip region, larger values of 2.71 nm ± 0.03 nm for the transition zone, and 2.66 nm ± 0.03 nm for the hair shaft, where the uncertainties originated from the Gaussian error distributions of the fits. The position of the equatorial 020 reflection also deviated most from the reference values of purified α-chitin (table 1).

No significant differences were found between the different sample preparations and setups. The reflection patterns were the same with only slight differences of the chitin *q*-values (table 1), and the exception that the 001 reflection was not observed in the previously frozen samples examined at the MiNaXS-beamline P03 at PETRA III. In these samples the additional non-chitin peak in the tip region was found at $q = 15.16$ nm^{-1}, compared to $q = 14.83$ nm^{-1} in the fresh samples examined at the ESRF. With the lower spatial resolution used at PETRA III, the 013 reflections of chitin fibres were detectable up to 1 μm from the very tip of the attachment seta.

The chitin structures suffered severe damage from continuous and long term exposure to the intense and focused X-rays as indicated by a clear decrease of the wide-angle diffraction signal intensity over time. Half-life of signal intensity measured on data from the ESRF for the 110 reflection was 6.9 s (figure S1*a*), and 6.5 s for the 020 reflection of the same hair. After 10 s of continuous exposure, the signal to noise ratio already decreased to levels not suited anymore for easy and proper analysis. Interestingly, the SAXS intensity slowly rose up to approximately 20 s exposure time, and increased quickly to approximately 5-fold the initial intensity value at 40 s exposure time of the same spot (figure S1*b*).

3.2. Mapping microtrich orientation using SAXS

Three areas sized 20 × 20 μm^2 and a smaller patch at the very tip were selected in the three different functional regions of the distal part of the attachment hair (figure 4). These areas were scanned with a resolution of 200 nm resulting in 10,201 diffraction patterns each. Orientation of the mesoscopic structures identified by small-angle X-Ray scattering coincided with the

longitudinal orientation of the microtrichs branching off the bulk hair shaft in all examined regions of the seta.

In the hair shaft region, fibre orientation determined using the SAXS signals clearly matched the physical orientation of single microtrichs on the ventral side of the seta. Dorsally single microtrichs could not be resolved. However, the orientation of the SAXS signals indicated the orientation of the overlapping microtrich rows that were simultaneously exposed to the X-ray beam at each pixel of the map (figure 4*a*).

In the transition zone the number of microtrichs per area increased and made identification of single structures more difficult, especially in the middle of the seta. On the dorsal side, the angular orientation of the microtrichs was approximately 20° off the long axis of the whole seta, and 30° to 40° to the opposite direction on the ventral side (figure 4*b*).

In the tip region, the SAXS signal orientation clearly differentiated between the dorsal and ventral microtrichs (figure 4*c*). Dorsally, the microtrichs pointed towards the dorsal side and were shifted to the seta long axis by an angle of approximately 10°. The stalks of the ventral microtrichs were oriented between 70° and 90° towards the ventral aspect of the hair. At the ventral boundary of the SAXS signal, a strip oriented approximately 10° to 20° different from the microtrich stalks likely showed the main orientation of the spatula-shaped adhesive contact elements in the tip region of the microtrichs (figure 4*c*).

3.3. Mapping of SAXS intensity

The full dimensions of the structures of the setae were best resolved by mapping the intensity distribution of the small-angle scattering signals (figure 5). In the shaft region, single long microtrichs could be resolved best on the ventral side of the hair. On the bulk hair shaft, several separated line-shaped structures with high intensity most likely corresponded to the branching sites of single long microtrichs. A single line of maximum intensity was located exactly at the boundary surface of the bulk shaft of the seta with air (figures 5*a,* 6*a*). In the bulk hair shaft of the transition zone, three lines with increased signal intensity were observed (figure 5*b*). They coincide with the two boundaries of the longitudinally oriented chitin-rich area of the bulk hair shaft of the transition zone, and the boundary of the bulk hair shaft with air as observed in the WAXS intensity maps (figure 6*b*).

Maximum SAXS intensities in the tip region (figure 5*c*) overlap with the area of the change of mesoscopic structures orientation, from along the seta's main axis to perpendicular to it (figure 4*c*), indicating that it most likely represents the bulk hair shaft and the area of branching of the microtrich rows in the broadest section of the brush-like hair tip structure

(compare figure 1*a*). Interestingly, increased SAXS intensity was also found in the region of the spatula-shaped structures at the tips of the microtrichs and likely indicated strong scattering of the X-ray beam by the thin and flat spatulae (figure 5*c*).

3.4. Chitin distribution and orientation

The intensity map of the wide-angle 013 chitin reflection of the hair shaft region clearly revealed the dimension of the bulk shaft of the seta with practically no diffraction signal from the microtrichs. The two walls of the bulk shaft of the seta pointed to a tube-shaped arrangement of this section. Interestingly, the diffraction intensity of the dorsal wall was higher than that of the ventral one, indicating higher chitin density and therefore stronger material of the dorsal wall compared with the ventral wall (figure 6*a*). In the transition zone, there was an approximately 500 nm thick line with high intensity of the 013 reflection located dorsally in the bulk shaft of the seta, too. Additionally, some 013 signal could be located in the region of branching microtrichs dorsal and ventral of the bulk shaft of the seta (figure 6*b*). In the tip region, the most intense 013 diffraction signal was measured in the core backbone structure narrowing towards the very tip. The signal intensity was clearly increased in the zone of microtrichs branching off the backbone. A slight chitin signal could be detected up to the tips of the microtrichs (figure 6*c*).

Mapping the intensity of the reflections in the q-range between 13 nm^{-1} and 16 nm^{-1} including the 110 chitin and the yet unidentified non-chitin signals was less selective in terms of identification of specific structures. In the shaft region the intensity of this mixed signal was more evenly distributed in the bulk material, and maximum intensity areas overlapped with those of the 013 chitin peaks in the wall region. Close to the bulk shaft of the seta, weak signals of the microtrich structures could be observed (figures 6*a*,*d*). In the transition zone, the area with the highest intensity of the mixed signal was found in the bulk hair shaft matching the backbone structure with increased small angle X-ray scattering intensity. Signals of branching microtrichs were observed dorsally and ventrally (figures 5*b*, 6*e*). In the tip region, the area of high intensity of the mixed wide-angle X-ray diffraction signal was larger than that of the 013 chitin peak. It was centred in the highest intensity region of the small-angle X-ray scattering intensity maps, and clearly showed the dimension of the bulk material backbone in the brush-region of the seta. Branching of microtrich rows and weak signals along the long axis of the microtrichs could be mapped up to the spatula region (figure 6*f*).

Orientation of the azimuthal 013 chitin reflection was mapped for the data points with sufficient signal intensity. In the hair shaft region and the transition zone, the orientation of the

crystalline chitin chains strictly followed the long orientation of the seta. Orientation along microtrichs was only found in single data points close to the bulk hair shaft (figure 7*a,b*). Orientation mapping in the tip region was difficult, most likely because of the three-dimensional overlap of many different structures and low signal-to-noise ratio. However, quite several single data points in the backbone region showed orientation along the long axis of the seta, and some in the microtrich branching region along the proposed long axis of the microtrichs (figure 7*c*).

4. Discussion

The lattice parameters indicating the physical dimensions of the orthorhombic unit cell were calculated from the positions of the chitin wide-angle reflections and are listed and compared with those of other chitin samples in table 2. The size of the crystalline unit cell, i.e. repeating distance, along the long axis of the polymer determined by parameter *c* was slightly larger than that of purified chitin and in the range found for chitin of the spider´s fang. Parameter *a* quantifying the distance between two nearest sheets of the same direction in one specific cross-section of the polymer´s long axis very well matched the values of deproteinised and purified α-chitin. Parameter *b* indicates the repeating distance between two chains with same orientation (each consisting of a pair of antiparallel chains running in opposite direction along the *c* axis) in the direction of the hydrogen bonds and showed the largest deviation from the reference values of purified α-chitin. Similar large values were also found in the spider´s fang [46]. For the determination of parameter *b*, the position of the equatorial 020 reflection, which differed strongest from the α-chitin reference value (table 1), was most important. The position and width of the 020 reflection varied in different sections of the seta (figure 3). According to the Scherrer equation, the widened peak in the tip region pointed to smaller crystal sizes. Compared with the 020 peaks of the hair shaft region and the transition zone at $q = 5.94$ nm^{-1} it was found shifted by -0.30 nm^{-1} to the smaller value of $q = 5.64$ nm^{-1} in the tip region.

Similar changes of reflection peaks were reported for cellulose and explained by an increased influence of crystal surface effects and distortions by surrounding materials, such as hemicelluloses, on the lattice of smaller crystals, leading to an increase of the lattice parameter in the weakest direction [53]. In chitin only four hydroxyl groups in each repeating unit are responsible for the *b*-directed hydrogen bonds between the single chains [54]. These hydrogen bonds of the unit cell are most susceptible for interactions with other molecules in the

surrounding, such as water and cuticular proteins. Consequently, apart from possible size-effects as in cellulose, the adsorption of water and cuticular proteins to the chitin chains could additionally explain the shift of the 020 peak and the deviation of *b* from purified chitin as discussed previously [47].

Minimum chitin crystal sizes of the different regions of the attachment seta were 2.59 nm ± 0.02 nm (error of the fit) in the tip, 2.71 nm ± 0.03 nm in the transition zone, and 2.66 nm ± 0.03 nm in the hair shaft (calculated from position and width of the reflection peaks using the Scherrer equation). These values were well within the range of the diameters between 2.5 nm and 3.0 nm found in the literature for the molecular chitin chains that are typically bundled to nanofibrils and wrapped by proteins [44,49].

Functionally different crystal sizes in the different sections of the attachment seta can be explained as follows. Smaller crystals in the tip region likely result in increased flexibility promoting contact formation with a surface and eventually adhesion. Similar mechanical effects, based on the transition from stiff to soft material in the tip, were previously reported for the attachment setae of coccinelid beetles [31]. When compared with the shaft region of the spider seta, which is mechanically reinforced against buckling by its tube-shaped hollow structure (figure 6*a*), the mechanically more stable larger cell size in the transition zone of the spider hair can be explained as adaptation to a proposed stress concentration in the narrowed backbone (figure 6*b*) upon contact of the seta with the substrate surface.

The origin of the reflection at q = 13.90 nm^{-1} in the shaft region (figure 2*a*) and the azimuthally widened reflection at q = 14.83 nm^{-1} in the tip region (figure 2*c*) finally remained unidentified. However, these reflections were likely caused by the protein matrix surrounding the chitin fibrils. Valverde Serrano et al. [47] found a similar peak at q = 13.89 nm^{-1} in the cuticle of dry intact leg tendons of *Cupiennius salei*, which disappeared upon deproteinisation, strongly pointing on its origin in the proteinaceous β-sheet motif. The high intensity of the proposed protein reflection in the tip region of the attachment seta can be explained by an increased amount of structural proteins making up the shapes of the many and highly ordered microtrichs.

The strict orientation of the chitin fibrils in parallel along the longitudinal axis of the attachment seta is remarkable (figure 7), especially in comparison with the arrangement of chitin fibres in other body parts, such as e.g. the leg cuticle, where the chitin fibrils are mostly arranged in a plywood manner of helicoidally rotating layers in parallel with the surface [42,46,55]. Alignment of chitinous fibres perpendicular to the surface was shown for the soft

adhesive pads of grasshoppers and locusts [56,57]. It was attributed to enhanced flexibility of the material under compression load, necessary for contact formation especially with uneven surfaces. For an animal, sitting on a vertical surface or upside-down, perpendicular orientation of the fibres can also be interpreted as an adaptation to the tensile forces that arise upon attachment. Most likely the same is true for the fibrils in the spider´s attachment hair, and the longitudinal orientation of the fibres reinforces the structure in the direction of the tensile forces that act when the animal sits on a vertical surface, which is the preferred resting position of *Cupiennius salei*.

The intensity of the identified chitin reflections in figure 7*a-c* corresponds to the density of chitin in the cuticle material. The chitin fibres reinforcing the cuticle can be interpreted as specifically distributed to maintain and reinforce the mechanical stability of the attachment setae. The larger chitin density in the dorsal wall of the hair shaft likely reinforces it against buckling, when the seta is pushed onto a surface. The less stiff ventral wall allows sufficient structural compliance, when the seta is pulled off. A similar mechanical behaviour can be proposed for the asymmetrically reinforced transition zone that by its shape is supposed to be more flexible. In the tip region, the backbone serves as the structure to hold several hundred microtrichs in place and showed the highest chitin content. In the region of the microtrichs, the wide-angle diffraction signal of chitin was weak, however, present up to the tip indicating that the stalk and likely also the spatula-shaped adhesive contact elements were chitin-reinforced. Summed up, it seems very likely that the strains and stresses that arise from the forces that act on the adhesive tip during attachment, adhesion in contact, and detachment at every step of the spider, are most evenly distributed by the arrangement pattern of the reinforcing chitin fibres to avoid material failure.

Using scanning nanofocus X-ray diffraction on a microscopic level allowed us finding yet unknown structures of the spider attachment hairs. Unique to X-ray diffraction was the possibility to specifically identify and localize the chitin fibres and their orientation within the cuticle of the attachment hair. In future experiments it would be interesting to attach and detach attachment hairs to a surface *in situ* in the scanning nanofocus X-ray diffraction setup, in order to quantify changes in fibre orientation in the adhesive tip and other regions of the seta. This will allow for further extraction of structure-function relationships for further improvement of novel biologically-inspired artificial structured adhesives.

Authors´ Contributions. CFS, MM, and SNG conceived of the study. CFS, AG, MB, MR, and CK designed the experiments. CFS and SF prepared the samples. CFS, SF, AG, IK, MB, MR, HS, CK, and MM carried out the beamtime work. SF, CFS, IK, AG, and MB evaluated the raw data. CFS, SF, and MM interpreted the data. CFS drafted the manuscript. SF contributed to drafting of the manuscript. SF, MM, and SNG commented on the draft of the manuscript. All authors gave final approval for publication.

Competing interests. We have no competing interests.

Funding. The allocation of beamtime and travel grants from ESRF to CFS, MM, SF, IK, AG, and HS and Helmholtz-Zentrum Geesthacht to CFS and AG are greatly acknowledged. The work of IK and AG was funded within the Helmholtz Virtual Institute "New X-ray analytic methods in materials science (VI-NXMM)" of the Helmholtz Association (HGF).

Acknowledgements. We acknowledge the European Synchrotron Radiation Facility for provision of synchrotron radiation facilities at beamline ID13. Parts of this research were carried out at MiNaXS beamline P03 of PETRA III at DESY, a member of the Helmholtz Association (HGF). We thank Emanuela Di Cola for assistance during a previous beamtime at the ESRF that led to the experimental setup of the present study, and Prof. Dr. Friedrich G. Barth and Wolfgang Kallina from the Department of Neurobiology of the University of Vienna, Austria, for supply with living spiders.

References

1. Homann H. 1957 Haften Spinnen an einer Wasserhaut? *Naturwissenschaften* **44**, 318–319. (doi:10.1007/BF00630926)
2. Roscoe DT, Walker G. 1991 The adhesion of spiders to smooth surfaces. *Bull. Brit. Arachnol. Soc.* **9**, 219–223.
3. Niederegger S, Gorb SN. 2006 Friction and adhesion in the tarsal and metatarsal scopulae of spiders. *J. Comp. Physiol. A* **192**, 1223–1232. (doi:10.1007/s00359-006-0157-y)
4. Wolff JO, Gorb SN. 2013 Radial arrangement of Janus-like setae permits friction control in spiders. *Sci. Rep.* **3**, 1101. (doi:10.1038/srep01101)
5. Gorb SN. 1998 The design of the fly adhesive pad: distal tenent setae are adapted to the delivery of an adhesive secretion. *Proc. R. Soc. Lond. B* **265**, 747–752. (doi:10.1098/rspb.1998.0356)
6. Geiselhardt SF, Lamm S, Gack C, Peschke K. 2010 Interaction of liquid epicuticular hydrocarbons and tarsal adhesive secretion in *Leptinotarsa decemlineata* Say (Coleoptera: Chrysomelidae). *J. Comp. Physiol. A* **196**, 369–378. (doi:10.1007/s00359-010-0522-8)
7. Dirks J-H, Federle W. 2011 Fluid-based adhesion in insects – principles and challenges. *Soft Matter* **7**, 11047. (doi:10.1039/c1sm06269g)
8. Kovalev AE, Filippov AE, Gorb SN. 2013 Insect wet steps: loss of fluid from insect feet adhering to a substrate. *J. R. Soc. Interface* **10**, 201206939. (doi:10.1098/rsif.2012.0639)

9. Gernay S, Federle W, Lambert P, Gilet T. 2018 Elasto-capillarity in insect fibrillar adhesion. *J. R. Soc. Interface* **13**, 20160371. (doi:10.1098/rsif.2016.0371)
10. Maderson PFA. 1964 Keratinized epidermal derivatives as an aid to climbing in gekkonid lizards. *Nature* **203**, 780–781. (doi:10.1038/203780a0)
11. Autumn K, Liang YA, Hsieh ST, Zesch W, Chan WP, Kenny TW, Fearing R, Full RJ. 2000 Adhesive force of a single gecko foot-hair. *Nature* **405**, 681–685. (doi:10.1038/35015073)
12. Autumn K, Sitti M, Liang YA, Peattie AM, Hansen WR, Sponberg S, Kenny TW, Fearing R, Israelachvili JN, Full RJ. 2002 Evidence for van der Waals adhesion in gecko setae. *P. Nat. Acad. Sci. U. S. A.* **99**, 12252–12256. (doi:10.1073/pnas.192252799)
13. Huber G, Gorb SN, Spolenak R, Arzt E. 2005 Resolving the nanoscale adhesion of individual gecko spatulae by atomic force microscopy. *Biol. Lett.* **1**, 2–4. (doi:10.1098/rsbl.2004.0254)
14. Rizzo NW, Gardner KH, Walls DJ, Keiper-Hrynko NM, Ganzke TS, Hallahan DL. 2006 Characterization of the structure and composition of gecko adhesive setae. *J. R. Soc. Interface* **3**, 441–451. (doi:10.1098/rsif.2005.0097)
15. Huber G, Orso S, Spolenak R, Wegst UGK, Enders S, Gorb SN, Arzt E. 2008 Mechanical properties of a single gecko seta. *Int. J. Mater. Res.* **99**, 1113–1118. (doi:10.3139/146.101750)
16. Alibardi L. 2018 Review: mapping proteins localized in adhesive setae of the tokay gecko and their possible influence on the mechanism of adhesion. *Protoplasma* **255**, 1785–1797. (doi:10.1007/s00709-018-1270-9)
17. Kesel AB, Martin A, Seidl T. 2003 Adhesion measurements on the attachment devices of the jumping spider *Evarcha arcuata*. *J. Exp. Biol.* **206**, 2733–2738. (doi:10.1242/jeb.00478)
18. Kesel AB, Martin A, Seidl T. 2004 Getting a grip on spider attachment: an AFM approach to microstructure adhesion in arthropods. *Smart Mater. Struct.* **13**, 512–518. (doi:10.1088/0964-1726/13/3/009)
19. Geim AK, Dubonos SV, Grigorieva KS, Novoselov KS, Zhukov AA, Shapoval SY. 2003 Microfabricated adhesive mimicking gecko foot hair. *Nature Mater.* **2**, 461–463. (doi:10.1038/nmat917)
20. Sitti M, Fearing RS. 2003 Synthetic gecko foot-hair micro/nano-structures as dry adhesives. *J. Adhes. Sci. Technol.* **18**, 1055–1073. (doi:10.1163/156856103322113788)
21. Yurdumakan B, Raravikar NR, Ajayan PM, Dhinojwala A. 2005 Synthetic gecko foot-hairs from multiwalled carbon nanotubes. *Chem. Commun.* **2005**, 3799–3801. (doi:10.1039/B506047H)
22. Ge L, Sethi S, Ci L, Ajayan PM, Dhinojwala A. 2007 Carbon nanotube-based synthetic gecko tapes. *P. Nat. Acad. Sci. U. S. A.* **104**, 10792–10795. (doi:10.1073/pnas.0703505104)
23. Lee H, Lee BP, Messersmith PB. 2007 A reversible wet/dry adhesive inspired by mussels and geckos. *Nature* **448**, 338–341. (doi:10.1038/nature05968)
24. Mahdavi A, Ferreira L, Sundback C, Nichol JW, Chan EP, Carter DJD, Bettinger CJ, Patanavanich S, Chignozha L, Ben-Joseph E, Galaktos A, Pryor H, Pomerantseva I, Masiakos P. T, Faquin W, Zumbuehl A, Hong S, Borenstein J, Vacanti J, Langer R, Karp JM. 2008 A biodegradable and biocompatible gecko-inspired tissue adhesive. *P. Nat. Acad. Sci. U. S. A.* **105**, 2307–2312. (doi:10.1073/pnas.0712117105)

25. Qu L, Dai L, Stone M, Xia Z, Wang ZL. 2008 Carbon nanotube arrays with strong shear binding-on and easy normal lift-off. *Science* **322**, 238–242. (doi:10.1126/science.1159503)
26. Boesel LF, Greiner C, Arzt E, del Campo A. 2010 Gecko-inspired surfaces: a path to strong and reversible dry adhesives. *Adv. Mater.* **22**, 2125–2137. (doi:10.1002/adma.200903200)
27. Chen B, Goldberg Oppenheimer P, Shean TAV, Wirth CT, Hofmann S, Robertson J. 2012 Adhesive properties of gecko-inspired mimetic via micropatterned carbon nanotube forests. *J. Phys. Chem.* **116**, 20047–20053. (doi:10.1021/jp304650s)
28. Schaber C F, Heinlein T, Keeley G, Schneider JJ, Gorb SN. 2015 Tribological properties of vertically aligned carbon nanotube arrays. *Carbon* **94**, 396–404. (doi:10.1016/j.carbon.2015.07.007)
29. Frost SJ, Mawad D, Higgins MJ, Ruprai H, Kuchel R, Tilley RD, Myers S, Hook JM, Lauto A. 2016 Gecko-inspired chitosan adhesive for tissue repair. NPG Asia Mater. 8, e280. (doi:10.1038/am.2016.73)
30. Peisker H, Michels J, Gorb SN. 2013 Evidence for a material gradient in the adhesive tarsal setae of the ladybird beetle *Coccinella septempunctata*. *Nat. Commun.* **4**, 1661. (doi:10.1038/ncomms2576)
31. Barth FG. 2002 *A spider´s world: senses and behavior*. Heidelberg: Springer. (doi:10.1007/978-3-662-04899-3)
32. McConney ME, Schaber CF, Julian MD, Barth FG, Tsukruk VV. 2007 Viscoelastic nanoscale properties of cuticle contribute to the high-pass properties of spider vibration receptor (*Cupiennius salei* Keys). *J. R. Soc. Interface* **4**, 1135–1143. (doi:10.1098/rsif.2007.1000)
33. Fratzl P, Barth FG. 2009 Biomaterial systems for mechanosensing and actuation. *Nature* **462**, 442–448. (http://dx.doi.org/10.1038/nature08603)
34. Politi Y, Pippel E, Licuco-Massouh ACJ, Bertinetti L, Blumtritt H, Barth FG, Fratzl P. 2017 Nano-channels in the spider fang for the transport of Zn ions to cross-link His-rich proteins pre-deposited in the cuticle matrix. *Arthropod Struct. Dev.* **46**, 30–38. (doi:10.1016/j.asd.2016.06.001)
35. Wohlfart E, Wolff JO, Arzt E, Gorb SN. 2014 The whole is more than the sum of all its parts: collective effect of spider attachment organs. *J. Exp. Biol.* **217**, 222–224. (doi:10.1242/jeb.093468)
36. Albert JT, Friedrich OC, Dechant H-E, Barth FG. 2001 Arthropod touch reception: spider hair sensilla as rapid touch detectors. *J. Comp. Physiol. A* **187**, 303–312. (doi:10.1007/s003590100202)
37. McConney ME, Schaber CF, Julian MD, Eberhardt WC, Humphrey JAC, Barth FG, Tsukrukl VV. 2009 Surface force spectroscopic point load measurements and viscoelastic modelling of the micromechanical properties of air flow sensitive hairs of a spider (*Cupiennius salei*). *J. R. Soc. Interface* **6**, 681–694. (doi:10.1098/rsif.2008.0463)
38. Schaber CF, Barth FG. 2015 Spider joint hair sensilla: adaptation to proprioreceptive stimulation. *J. Comp. Physiol. A* **201**, 235–248. (doi:10.1007/s00359-014-0965-4)

39. Barth FG. 2016 A spider´s sense of touch: what to do with myriads of tactile hairs? In *The ecology of animal senses* (eds G von der Emde, E Warrant), pp. 27–58. Cham: Springer. (doi:10.1007/978-3-319-25492-0_2)
40. Gorb SN. 2001 *Attachment devices of insect cuticle*. Dordrecht: Springer. (doi:10.1007/0-306-47515-4)
41. Wolff JO, Gorb SN. 2012 Surface roughness effects on attachment ability of the spider *Philodromus dispar* (Araneae, Philodromidae). *J. Exp. Biol.* **215**, 179–184. (doi:10.1242/jeb.061507)
42. Barth FG. 1973 Microfiber reinforcement of an arthropod cuticle. *Z. Zellforsch.* **144**, 409–433. (doi:10.1007/BF00307585)
43. Minke R, Blackwell J. 1978 The structure of α-chitin. *J. Mol. Biol.* **120**, 167–181. (doi:10.1016/0022-2836(78)90063-3)
44. Neville AC, Parry DAS, Woodhead-Galloway J. 1976 The chitin crystallite in arthropod cuticle. *J. Cell. Sci.* **21**, 73–82.
45. Politi Y, Priewasser M, Pippel E, Zaslansky P, Hartmann J, Siegel S, Li C, Barth FG, Fratzl P. 2012 A spider´s fang: how to design an injection needle using chitin-based composite materials. *Adv. Funct. Mater.* **22**, 2519–2528. (doi:10.1002/adfm.201200063)
46. Erko M, Hartmann MA, Zlotnikov I, Valverde Serrano C, Fratzl P, Politi Y. 2013 Structural and mechanical properties of the arthropod cuticle: comparison between the fang of the spider *Cupiennius salei* and the carapace of American lobster *Homarus americanus*. *J. Struct. Biol.* **183**, 172–179. (doi:10.1016/j.jsb.2013.06.001)
47. Valverde Serrano C, Leemreize H, Bar-On B, Barth FG, Fratzl P, Zolotoyabko E, Politi Y. 2016 Ordering of protein and water molecules at their interfaces with chitin nano-crystal. *J. Struct. Biol.* **193**, 124–131. (doi:10.1016/j.jsb.2015.12.004)
48. Vincent JFV, Wegst UGK. 2004 Design and mechanical properties of insect cuticle. *Arthropod Struct. Dev.* **33**, 187–199. (doi:10.1016/j.asd.2004.05.006)
49. Raabe D, Al-Sawalmih A, Yi SB, Fabritius H. 2007 Preferred crystallographic texture of α-chitin as a microscopic and macroscopic design principle of the exoskeleton of the lobster *Homarus americanus*. *Acta Biomater.* **3**, 882–895. (doi:10.1016/j.actbio.2007.04.006)
50. Krywka C, Neubauer H, Priebe M, Salditt T, Keckes J, Buffet A, Roth SV, Doehrmann R, Mueller M. 2012 *J. Appl. Cryst.* **45**, 85–92. (doi:10.1107/S0021889811049132)
51. Azaroff, LV. 1968 *Elements of X-Ray Crystallography*. New York, NY: McGraw-Hill.
52. Sikorski P, Hori R, Wada M. 2009 Revisit of a-chitin crystal structure using high resolution X-ray diffraction data. *Biomacromolecules* **10**, 1100–1105. (doi:10.1021/bm801251e)
53. Müller M, Murphy B, Burghammer M, Riekel C, Pantos E, Gunneweg J. 2007 Ageing of native cellulose fibres under archaeological conditions: textiles from the Dead Sea region studied using synchrotron X-ray microdiffraction. *Appl. Phys. A* **89**, 877–881. (doi:10.1007/s00339-007-4219-y)
54. Friák M, Fabritius H-O, Nikolov S, Petrov M, Lymperakis L, Sachs C, Elstnerová P, Neugebauer J, Raabe D. 2013 *Multi-scale modelling of a biological material: the arthropod exoskeleton.* In

Materials design inspired by nature: function through inner architecture (eds P. Fratzl, JWC Dunlop, R Weinkamer), pp. 197–218. Cambridge, UK: Royal Society of Chemistry. (doi:10.1039/9781849737555-00197)

55. Hößl B, Böhm HJ, Schaber CF, Rammerstorfer FG, Barth FG. 2009 Finite element modeling of arachnid slit sensilla: II. Actual lyriform organs and the face deformations of the individual slits. *J. Comp. Physiol. A* **195**, 881–894. (doi:10.1007/s00359-009-0467-y)
56. Gorb S, Jiao Y, Scherge M. 2000 Ultrastructural architecture and mechanical properties of attachment pads in *Tettigonia viridissima* (Orthoptera Tettigoniidae). *J. Comp. Physiol. A* **186**, 821–831. (doi:10.1007/s003590000135)
57. Perez Goodwyn P, Peressadko A, Schwarz H, Kastner V, Gorb S. 2006 Material structure, stiffness, and adhesion: why attachment pads of the grasshopper (*Tettigonia viridissima*) adhere more strongly than those of the locust (*Locusta migratoria*) (Insecta: Orthoptera). *J. Comp. Physiol. A* **192**, 1233–1243. (doi:10.1007/s00359-006-0156-z)

Table 1. Peaks of the diffraction vector q of the α-chitin fibre diffraction pattern of the attachment hairs and reference values

reflection peak	020 (nm^{-1})	110 (nm^{-1})	001 (nm^{-1})	012 (nm^{-1})	013 (nm^{-1})	004 (nm^{-1})
shaft*	5.90 ± 0.02	13.57 ± 0.01	6.23 ± 0.01	12.35 ± 0.01	18.63 ± 0.01	24.52 ± 0.01
tip region**	6.39 ± 0.23	13.78 ± 0.15	-	12.32 ± 0.07	18.59 ± 0.04	24.52 ± 0.08
lobster tendon*** [43]	6.62	13.54	6.14	12.27	18.59	24.54
crab tendon*** [52]	6.65	13.68		12.57	18.51	24.35

* fresh sample (data from beamtime at the ESRF); values from average diffraction pattern based on 1,853 single diffraction patterns ± error of the fit (N=1)

** previously frozen sample (data from beamtime at PETRA III); number of diffraction patterns n used for calculation of the mean values ± standard deviations (s. d.): 020: n=17, 110: n=38, 012: n=41, 013: n=41, 004: n=22 (N=1)

*** deproteinised

Table 2. Lattice parameters *a*, *b*, and *c* of the orthorhombic unit cell of chitin in the attachment hair, a leg tendon, and the fang of *Cupiennius salei*, and reference values from purified chitin samples

Sample	*a* (nm)	*b* (nm)	*c* (nm)
Cupiennius salei attachment hair*	0.474 ± 0.003	2.131 ± 0.03	1.023 ± 0.002
C. salei tendon** [47]	0.470	1.897	1.028
C. salei fang [46]	0.46	2.06	1.02
lobster tendon*** [43]	0.474	1.886	1.032
crab tendon*** [52]	0.474	1.884	1.031

* based on shaft values of table 1

** intact dry

*** deproteinised

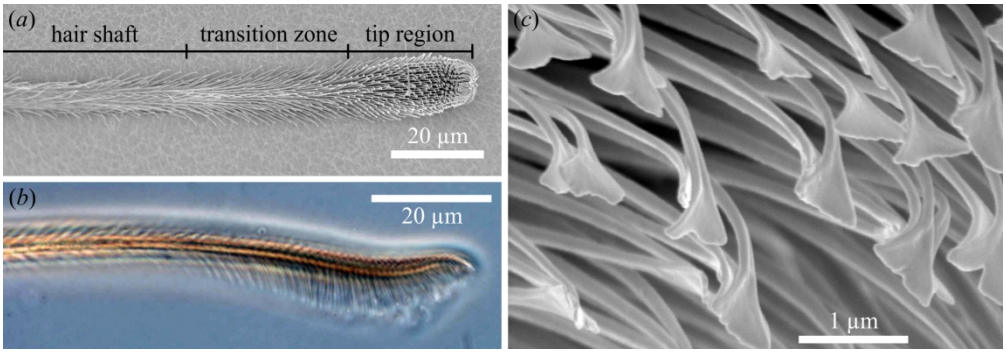

Figure 1. Morphology of the distal part of an attachment hair of the spider *Cupiennius salei*. (*a*) Scanning electron micrograph, ventral view. The terminology for the different sections corresponds to the presence of differently shaped microtrichs branching off the shaft of the seta. (*b*) Phase-contrast transmitted light micrograph, lateral view. In the tip region, the elongated microtrichs are oriented approximately perpendicular to the long axis of the seta and form a brush-like structure. (*c*) Scanning electron micrograph in the tip region. The spatula-shaped terminal elements of the microtrichs are the contact elements responsible for the spider's adhesion.

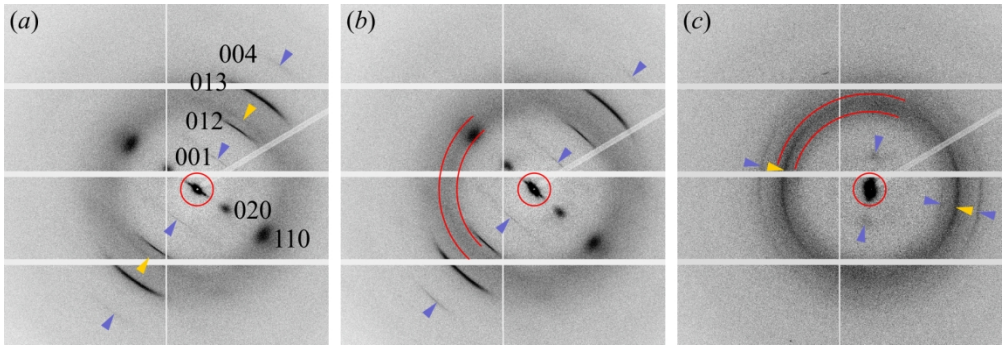

Figure 2. Averaged X-ray diffraction patterns from different regions of the attachment hair (data from beamtime at the ESRF). (*a*) Hair shaft, (*b*) transition zone, (*c*) tip region. The more sharp wide-angle scattering signals correspond to the equatorial 020, and 110, the meridional 001, and 004, and the 012 and 013 reflections of fibrous α-chitin. The open red circles indicate the range of small-angle scattering signals. The red sector lines in (*b*) and (*c*) delimit the range of *q*-values between 13 nm^{-1} and 16 nm^{-1} that was used for integration of the halo. Blue arrowheads point to weaker chitin signals as a guide for the eye. Yellow arrowheads point to the yet unidentified non-chitin reflections. Note that the longitudinal orientation of the crystalline chitin chains is perpendicular to the equator of the XRD/WAXS signals, and the longitudinal orientation of larger mesoscopic structures is perpendicular to the long axis of the SAXS signals.

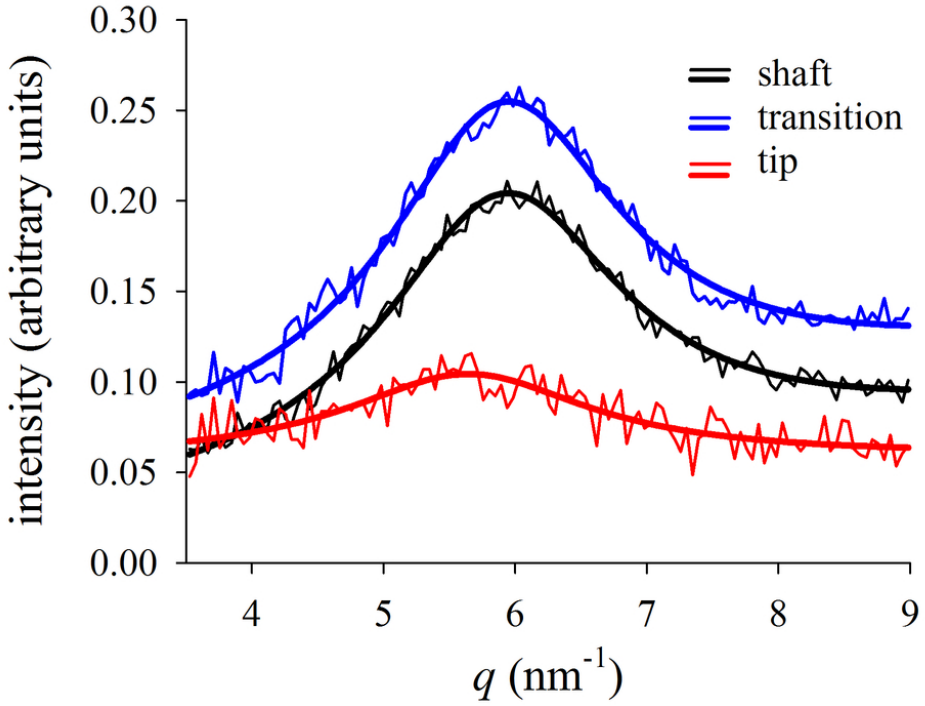

Figure 3. Peak of the wide-angle 020 diffraction signal of chitin in different functional regions of the attachment seta. The thicker lines are Lorentz peaks fitted to measured data (thinner lines).

82x69mm (300 x 300 DPI)

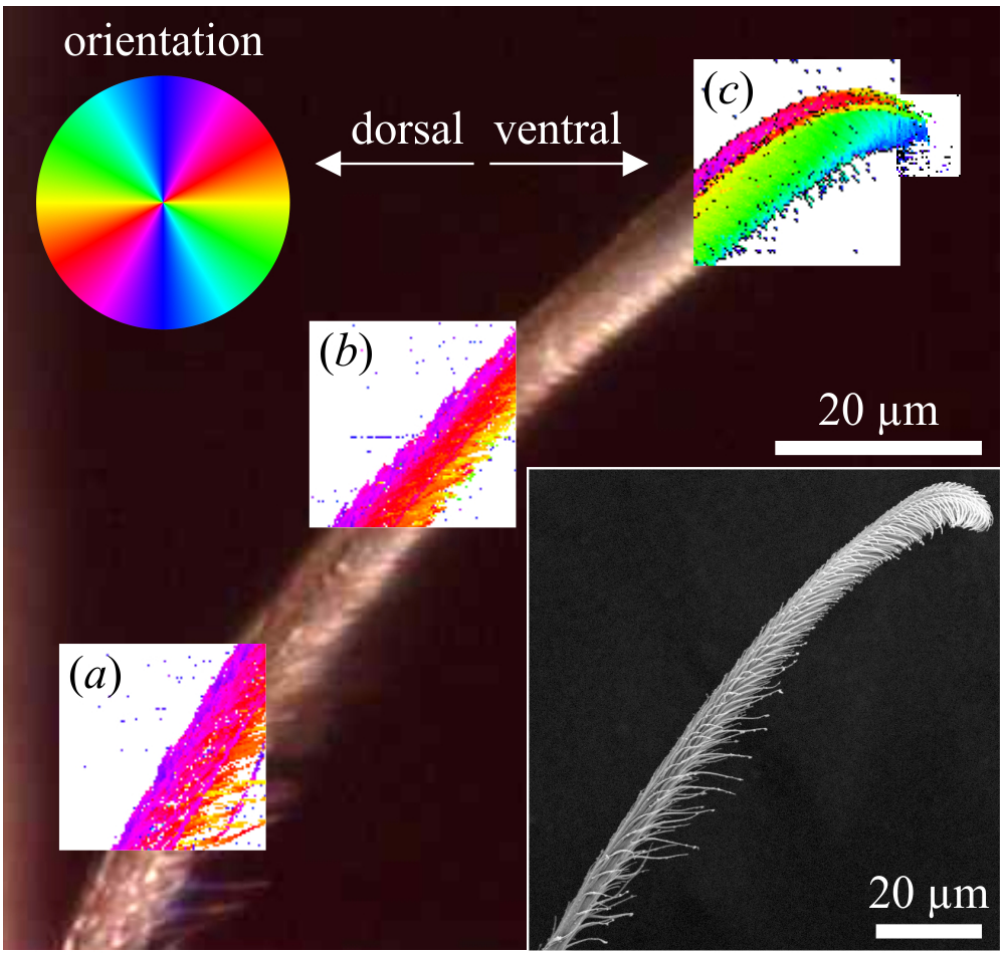

Figure 4. Maps of orientation of mesoscopic structures (sized ~100 nm) based on the SAXS signal's main orientation in different regions of the attachment seta. The angle of the mesoscopic structures corresponds to the orientation of the colours of the colour circle. (*a*) Hair shaft, (*b*) transition zone, (*c*) tip region. The background image for the overlaid maps is an optical micrograph of the actual position of the seta in the experimental setup. The inset shows a scanning electron micrograph of the seta long after the X-ray experiments. In the living spider, a substrate surface to attach to would be oriented vertically on the right side of the images.

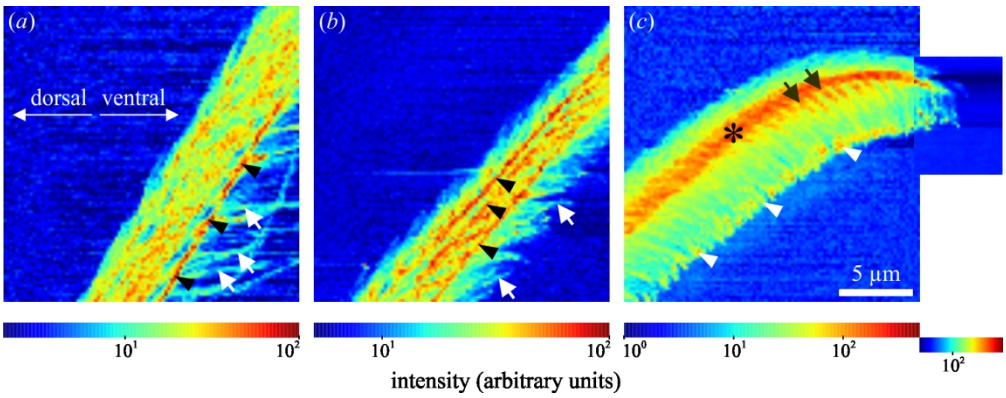

Figure 5. Small-angle X-ray scattering intensity maps. (*a*) Shaft region, (*b*) transition zone, (*c*) tip region, as shown in figure 4. In each map, the intensity range was adjusted for the maximum contrast as indicated by the colour bars. The arrows in (*a*) point to clearly visible single microtrichs, and the arrowheads to a line with increased intensity at the edge of the bulk hair shaft. In the transition zone (*b*), the arrows indicate single microtrichs. Arrowheads point to several lines with increased intensity oriented along the hair's long axis. In the tip region (*c*), the most intense scattering signal was measured in a backbone-like structure (asterisk), from which the rows of microtrichs branch off (arrows). Arrowheads point to the intense scattering in the spatula region of the microtrichs.

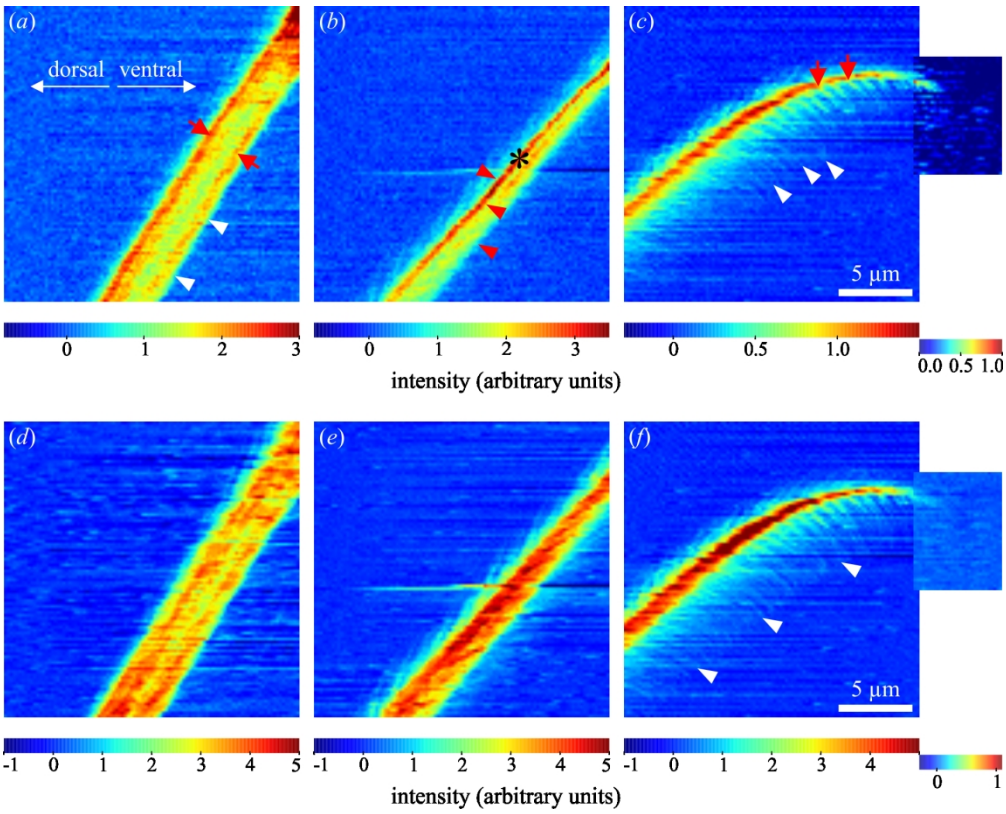

Figure 6. Wide-angle X-ray diffraction/scattering intensity maps. In each map, the intensity range was adjusted for maximum contrast as indicated by the colour bars. Upper line: Intensity of the 013 chitin reflection. (*a*) Hair shaft; the arrows point to the walls of the probably hollow shaft, and the arrowheads point to the edge of the seta at the same position as the line of increased small-angle scattering in figure 5*a*. (*b*) Transition zone; arrowheads correspond to the positions of the lines of increased small-angle scattering in figure 5*b*. The asterisk marks the line of the most intense chitin signal. (*c*) Tip region; arrows indicate rows of microtrichs branching off the backbone. Arrowheads indicate the outreach of the 013 signal following the microtrichs. Lower line: Intensity of the WAXS signal integrated between q-values of 13 nm^{-1} and 16 nm^{-1} (halo including parts of the 110 reflection of chitin and the yet unidentified non-chitin signals). (*d*) Hair shaft, (*e*) transition zone, (*f*) tip region. The arrowheads in (*f*) are at the same position as in figure 5*c* and illustrate the length of the microtrichs.

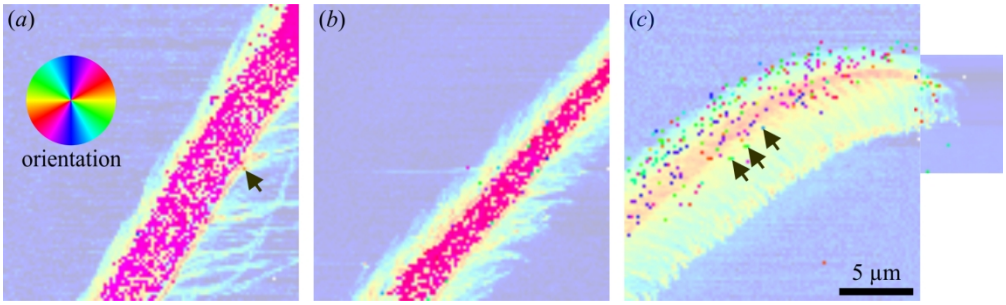

Figure 7. Orientation maps of the 013 wide-angle X-ray diffraction/scattering reflection showing the orientation of crystalline chitin as indicated by the colour circle. The SAXS intensity maps are plotted in the background. (*a*) Note the strict orientation of the signal along the long axis of the hair shaft. The arrow points to a single position, where the orientation follows a branching microtrich. (*b*) Transition zone. (*c*) Multiply oriented chitin crystals in the tip region. The arrows point to positions, where the orientation appears to match the longitudinal axis of the microtrichs.

Hierarchical architecture of spider attachment setae reconstructed from scanning nanofocus X-ray diffraction data

(doi:10.1098/rsif.2018.0692)

Clemens F. Schaber[1], Silja Flenner[2,3], Anja Glisovic[3], Igor Krasnov[3], Martin Rosenthal[4], Hergen Stieglitz[2,3], Christina Krywka[2], Manfred Burghammer[4], Martin Müller[2,3], Stanislav N. Gorb[1]

[1] Functional Morphology and Biomechanics, Zoological Institute, Kiel University, 24098 Kiel, Germany
[2] Helmholtz-Zentrum Geesthacht, Postfach 1160, 21494 Geesthacht, Germany
[3] Institute of Experimental and Applied Physics, Kiel University, 24098 Kiel, Germany
[4] European Synchrotron Radiation Facility (ESRF), CS 40220, 38043 Grenoble Cedex 9, France

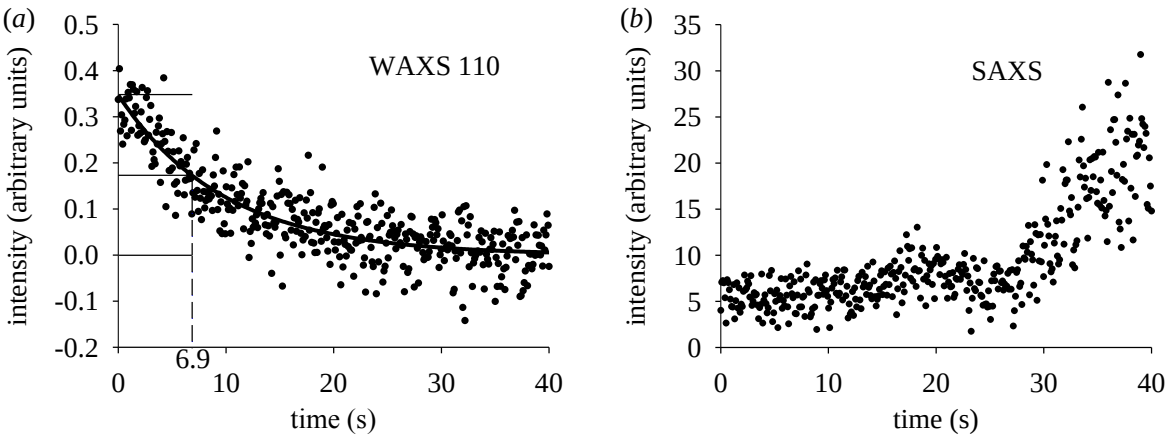

Figure S1. Modification of the X-ray diffraction signal intensity at 400-fold successive exposure by 0.1 s of an attachment hair to the focused X-ray beam at the ESRF. (*a*) Decrease of the equatorial 110 chitin wide-angle diffraction reflection. The exponential fit yields a half-life of signal intensity of 6.9 s exposure as indicated by the dashed line. The data points are shifted to the zero line of the asymptotic line fit. Negative intensity values are caused by subtraction of the background signal. (*b*) Increase of the SAXS signal intensity.